Iron persistence in a distal hydrothermal plume supported by dissolved-particulate exchange

Jessica N. Fitzsimmons[1,2], Seth G. John[3,4], Christopher M. Marsay[4,5], Colleen L. Hoffman[6], Sarah L. Nicholas[7,8], Brandy M. Toner[6,7], Christopher R. German[9], Robert M. Sherrell[1,10]

[1] Department of Marine and Coastal Sciences, Rutgers University, New Brunswick, NJ 08901, USA

[2] Department of Oceanography, Texas A&M University, College Station, TX, 77843, USA; jessfitz@tamu.edu

[3]Department of Earth Sciences, University of Southern California, Los Angeles, CA, USA; sethjohn@usc.edu

[4]Department of Earth and Ocean Sciences, University of South Carolina, Columbia, SC, USA

[5]Skidaway Institute of Oceanography, University of Georgia, Savannah, GA, USA; christopher.marsay@skio.uga.edu

[6]Department of Earth Science, University of Minnesota – Twin Cities, St. Paul, MN, USA; hoff0800@umn.edu

[7]Department of Soil, Water, and Climate, University of Minnesota – Twin Cities, St. Paul, MN, USA; toner@umn.edu

[8]Department of Earth and Ocean Sciences, National University of Ireland, Galway, Ireland; sarah.nicholas@nuigalway.ie

[9]Department of Geology & Geophysics, Woods Hole Oceanographic Institution, Woods Hole, MA, USA; cgerman@whoi.edu

[10]Department of Earth and Planetary Sciences, Rutgers University, Piscataway, NJ, USA; sherrell@marine.rutgers.edu

First Paragraph

Hydrothermally-sourced dissolved metals have been recorded in all ocean basins. In the oceans' largest known hydrothermal plume, extending westward across the Pacific from the Southern East Pacific Rise, dissolved iron and manganese were shown by the GEOTRACES program to be transported halfway across the Pacific. Here, we report that particulate iron and manganese in the same plume also exceed background concentrations, even 4000 km from the source. Both dissolved and particulate iron deepen by more than 350 m relative to ^{3}He – a non-reactive tracer of hydrothermal input – crossing isopycnals. Manganese shows no similar descent. Individual plume particle analyses indicate that particulate iron occurs within low-density organic matrices, consistent with its slow sinking rate of 5-10 m $year^{-1}$. Chemical speciation and isotopic composition analyses reveal that particulate iron consists of Fe(III) oxyhydroxides, while dissolved iron consists of nanoparticulate Fe(III) oxyhydroxides and an organically-complexed iron phase. The descent of plume dissolved iron is best explained by reversible exchange onto slowly sinking particles, likely mediated by organic compounds binding iron. We suggest that in ocean regimes with high particulate iron loadings, dissolved iron fluxes may depend on the balance between stabilization in the dissolved phase and the reversibility of exchange onto sinking particles.

High temperature vents spanning diverse geologic settings emit fluids enriched in dissolved Fe (dFe) and Mn (dMn), often a million times more concentrated than background deep ocean concentrations[1]. In the surface ocean, Fe is an essential[2], often limiting micronutrient for primary producers. Historically, global-scale studies have focused on atmospheric dust and continental margins as primary Fe sources[3], while hydrothermally-sourced Fe was expected to precipitate quantitatively into solid phases that settled onto underlying sediments close to vent sources, as polymetallic sulfides or oxyhydroxides following the rapid oxidation of Fe(II)[1,4]. Consequently, it was assumed that hydrothermal vents supply negligible dFe to the oceans[5].

More recently, however, distributions of dissolved metals, including measurements from several GEOTRACES studies, have confirmed the long-range transport of hydrothermally-sourced dFe from mid-ocean ridge sources into the interior of the Pacific[6-8], Atlantic[9,10], Indian[11], Southern[12,13], and Arctic[14] Oceans. Candidate stabilization mechanisms for hydrothermally-sourced dFe include the formation of small inorganic nanoparticles in the colloidal size fraction[15-17] and complexation by organic ligands that protect dFe from precipitation and gravitational settling[18-20]. For particulate metals, hydrothermal research has emphasized processes proximal to vent sources. Only one study reported pFe along the core of a westward-dispersing ^{3}He plume[21] overlying a region of metalliferous sediment enrichments near 15°S[22], but sampling extended only ~80 km off-axis. Thus, the transformations and lateral extent of particulate metals in distal hydrothermal plumes have been comparatively overlooked.

A major goal of the U.S. GEOTRACES GP16 East Pacific Zonal Transect was to determine the long-range fate of trace elements released by venting along the 15°S EPR plume trajectory.

Eleven full-depth stations were sampled over a ~4300 km transect starting at the SEPR ridge-axis (15°S, 112.75°W) and extending along the core of the largest known hydrothermal ^{3}He plume globally[23]. Because it is chemically inert, $^{3}He_{xs}$ ("xs" is non-atmospheric ^{3}He; see Methods) mixes conservatively during transport through the deep ocean, providing an unambiguous tracer of hydrothermal input[23]. Recently, a study of dissolved metals along the GP16 section showed that hydrothermally sourced dFe and dMn were transported along the entire plume length and that, despite anticipated scavenging, dFe was apparently conserved over much of the plume's length[8].

Here, we report complementary particulate Fe and Mn distributions across the same section (Figure 1). We also highlight the previously unreported deepening of dFe relative to isopycnals and ^{3}He and infer from isotope and synchrotron speciation techniques that this vertical descent of dFe is mediated by reversible exchange with a sinking pFe phase that, we argue, is likely facilitated by Fe associations with organic matter (Figure 2). Manganese, in contrast, does not sink across isopycnals, due to the association of pMn with low-density microbial capsules as well as the lack of organic and colloidal speciation for dMn, which we argue inhibits exchange with sinking particle phases. This decoupling of Fe and Mn has important implications for the fate of other elements in hydrothermal plumes and the scavenging removal of Fe from the global ocean.

Particulate hydrothermal plume – The hydrothermal plume was detectable across the entire ~4300 km transect from elevated particulate (>0.45 μm) Fe and Mn above ambient deep Pacific concentrations (Figure 1). This is by far the most extensive particulate hydrothermal plume ever documented, complementing the ^{3}He, dFe, and dMn plume distributions reported

97 previously[8]. Yet, both Fe- and Mn-rich particles must undergo aggregative removal from this
98 plume because they showed exponential loss, from plume depths, that greatly exceeded
99 dilution with particle-poor ambient deep Pacific water (quantified from $^{3}He_{xs}$ dilution; Figure 3).
100 For example, >90% of pFe was lost within the first 200 km off-axis, while $^{3}He_{xs}$ decreased by just
101 2-3 fold across the entire section (Figure 2). Overall, pFe and pMn loss was consistent with first
102 order kinetic removal (Figure S2), suggesting aggregation onto biogenic and/or lithogenic
103 particles settling from above at nearly constant rates[24] along the length of the plume. However,
104 near-field (<100 km) particles were removed too rapidly to fit a single exponential function
105 (Figure 2), suggesting that additional self-aggregation at higher particle concentrations in the
106 near-field environment leads to more rapid removal from the proximal plume (Figures 2, S2).
107 Regional advection rates near 15°S at ~2500 m, estimated from circulation models and
108 float observations, are 0.2-0.5 cm/s[25,26], yielding plume transport times from the ridge axis (Sta.
109 18) to Sta. 36 of 25-70 years. The anomalously low Fe, Mn, and ^{3}He concentrations at Sta. 23
110 (Figure 1) reflect an interruption of the continuous plume, perhaps due to anticyclonic
111 recirculation at 112-125°W[26]; this feature will not be discussed further in this paper.
112 Importantly, the pFe maximum deepened progressively, by ~350 m relative to
113 conservative $^{3}He_{xs}$ over the plume length, crossing isopycnals, (Figures 1, 4a; S3). This implies
114 that persistent hydrothermal pFe sinks slowly at ~5-10 m/yr (0.01-0.03 m/d), consistent with
115 Stokesian settling of ~0.5 μm pure ferrihydrite grains.
116 In contrast, pMn showed no gravitational settling behavior (Figures 1, 4b). Instead, peak
117 pMn concentrations remained close in depth to dMn and $^{3}He_{xs}$ and followed density surfaces,
118 indicative of isopycnal mixing. Thus, while most pMn and pFe are removed exponentially from

the plume by aggregation in/onto sinking particles (Figure 3), the vertical positions of the persistent pFe and pMn plumes decouple during transport down-plume (Figures 1, 2), suggesting that Fe- and Mn-bearing particles must differ fundamentally in size, shape, and/or specific gravity.

Chemical and isotopic composition of Fe-rich particles – Scanning Transmission X-ray Microscopy (STXM) and Fe 2p X-ray Absorption Near-Edge Structure (XANES) analyses showed that SEPR pFe is composed predominantly of Fe(III) oxyhydroxides (Figure 5), with little evidence for Fe(II) particles, even directly above the ridge axis. Images obtained from STXM also revealed the morphology of Fe-rich particles in the plume. Within 100 km of the SEPR (Sta. 18-20), the Fe-bearing particles consisted of Fe(III) oxyhydroxides largely co-located with organic matter in ~5-10 μm aggregates (Figure 5, a-c), similar to near-field hydrothermal Fe(II) from 9°N EPR[27]. Beyond ~100-200 km off-axis at 15°S EPR, however, the physicochemical form of hydrothermal pFe exhibited a marked morphological transition to discrete Fe(III) oxyhydroxide minerals embedded within a matrix of organic carbon (Figure 5, d-f) with much lower optical density. We infer from these results that the high specific gravity of any embedded Fe minerals is offset by the low specific gravity of associated organic matter, resulting in a low overall specific gravity. This allows large Fe-bearing hydrothermal particles to persist within a distinct hydrothermal plume for decades and over thousands of kilometers (Figures 1, 2) instead of settling rapidly at the Stokesian rates that would be predicted for pure ferrihydrite (e.g. ~750 m/y for 5 μm spheres in the proximal plume, Fig. 5).

Why doesn't pMn also settle across isopycnals in the distal plume? Prior work has shown that Mn uptake into hydrothermal plume particles is dominated by microbially

catalyzed[28,29] dissolved Mn(II) oxidation (otherwise kinetically inhibited[30]), yielding Mn oxide coatings on bacterial cells. Pure birnessite (ρ=2.9 g/cm^3) of bacterial-capsule size (~1 μm) would settle at ~18 m/y, but we hypothesize that the lower specific gravity of such bacterial capsules, even with MnO_2 coatings, prevents the settling of persistent pMn across isopycnals, thus mimicking dMn and $^3He_{xs}$ across the section. Future synchrotron investigations of the physicochemical speciation of hydrothermal pMn should test this hypothesis.

The isotopic composition of 'ligand-leachable' pFe (δ^{56}Fe) was nearly-constant across the plume (-0.25±0.14‰, 1σ SD; Figure 6a), even as pFe concentrations decreased ~1000-fold by aggregative removal and dilution. This suggests that hydrothermally-sourced pFe speciation is preserved down-plume, consistent with microprobe Fe XANES results beyond Sta. 21[31]. Most chemical reactions that would alter pFe speciation are associated with isotopic fractionation that ranges from a few tenths up to several ‰[32]. The observed variations in particulate δ^{56}Fe are smaller than would be predicted even for a reaction with an isotope effect as small as 0.1‰ (Figure 6a). This supports our earlier inferences (i) that pFe is removed by non-fractionating, aggregative sinking and (ii) that persistent hydrothermal pFe speciation experiences no further fractionating transformations during plume advection. The slightly heavier particulate δ^{56}Fe (-0.13 ±0.14‰) at the most distal end of our study (Sta. 30-36) indicates the contribution of isotopically heavier, background deep-ocean pFe at significant mixing ratios as hydrothermal pFe concentrations decreased (Figures 1, S1).

The physicochemical form of hydrothermal dissolved iron - A key finding of this study, not discussed previously[8] but critical to the fate of Fe in the SEPR hydrothermal plume, is that the maximum *dissolved* Fe also deepens by ~350 m by Sta. 36, mimicking pFe (Figures 1, 4a).

We attribute this previously undescribed phenomenon to reversible exchange between dFe and pFe on a rapid timescale relative to pFe sinking. This exchange must occur while apparently conserving total dFe inventories in the plume (Figure 3).

To investigate the chemical mechanism of this reversible exchange and resulting dFe descent, we examined the physicochemical speciation of dissolved Fe in the plume. Ultrafiltration (Figure S4) revealed that plume dFe (<0.2 μm, operationally)comprised mostly colloidal species (0.003-0.2 μm; 63±10% of dFe), while non-hydrothermal abyssal dFe is ~50% colloidal[10]. In contrast, dMn was predominantly truly soluble (<0.003 μm; 98±2%, Figure S4). While the chemical speciation of Fe in hydrothermal colloids is not yet known and may include inorganic compounds or organic complexation[10,33], colloids may be important for the stabilization of hydrothermal plume dFe.

Our δ^{56}Fe measurements showed that hydrothermal plume dFe resides in two chemical forms. In the young, near-field plume (Sta. 18, dFe >5 nM), mean δ^{56}Fe was -0.19 ±0.05‰ (1σ SD, n=4; Figure 6b), matching δ^{56}Fe values for pFe down-plume (-0.25±0.14‰; Figure 6a). Combined with our ultrafiltration results (Figure S4), this suggests that near-field dFe is dominated by inorganic Fe(III) oxyhydroxides of predominantly colloidal size. However, pure Fe-oxyhydroxide colloids (ρ=4.25 g/cm^3, ≤0.2 μm) should only sink 30-90 m during the 25-70 year transit down-plume by Stokesian settling, much less than the observed ~350 m deepening.

Moving westward down-plume, dFe concentrations decreased while dissolved δ^{56}Fe increased (Figure 6b). This trend was inverse modeled as simple two-component isotope mixing, between a proximal nanoparticulate Fe oxyhydroxide end-member with decreasing concentrations down-plume but fixed δ^{56}Fe = -0.19‰, and an invariant second end-member

185 modeled from average Sta. 32 values of [dFe] = 0.77 nM and δ^{56}Fe = +0.66‰. This model
186 revealed that our dissolved δ^{56}Fe data are best described by a nanoparticulate Fe oxyhydroxide
187 phase, diminishing down-plume and mixing into a constant, isotopically heavy dFe phase. What
188 is the chemical composition of the distal 0.77 nM, isotopically heavy dFe? It cannot be
189 nanopyrite because precipitated Fe(II) should be isotopically light[34]. Instead, we infer that this
190 non-oxyhydroxide dFe pool consists of organically-bound Fe(III), which is known to be
191 isotopically heavy relative to unbound Fe(III)[35,36]. The ligand-bound end-member is higher in
192 dFe concentration and heavier in isotopic composition than estimates of non-hydrothermal
193 background Pacific dFe from throughout the Pacific (~0.45±0.5nM[37], -0.10 to -0.22‰[38,39]),
194 including "upstream" of the SEPR (~GP16 Sta. 15: ~0.5 nM, δ^{56}Fe ~+0.4‰). Thus we conclude
195 that the plume beyond Sta. 32 consists of background deep Pacific Fe (~0.5 nM) plus an
196 organically-bound dFe fraction of hydrothermal origin (~0.3 nM, δ^{56}Fe > +0.66‰); dissolved-
197 phase nanoparticulate Fe oxyhydroxides compose ≤10% of dFe in the far-field hydrothermal
198 plume (Figure 2).
199 The composition and source of the inferred organic ligands are unknown but could
200 derive from excess unbound Fe ligands that are present throughout the deep ocean[40], from
201 bacterial release specific to hydrothermal plume environments[41], or through release from near-
202 vent chemoautotrophs and subsequent entrainment into buoyant plumes[42]. Regardless, we
203 propose that the hydrothermally-derived, organically-complexed, and isotopically heavy dFe
204 phase is pervasive throughout the plume but that because of its low concentration (~0.3 nM), it
205 is not isotopically resolvable in the near-field plume (dFe >5 nM).

Reversible exchange between dissolved and particulate Fe - If plume dFe is physically partitioned into soluble and colloidal fractions and chemically partitioned into a near-field nanoparticulate Fe oxyhydroxide phase superimposed on a near-constant background of hydrothermally-derived ligand-bound dFe, how can we explain the along-plume descent of dFe that mimics the sinking of the pFe maximum? Simple disaggregation of pFe into nanoparticulate dFe during pFe settling would require injection of substantial concentrations of dFe with light δ^{56}Fe (-0.2‰), but this was not observed: dFe became heavier down-plume (Figure 6b) and total dFe was apparently conserved (Figure 3).

Instead we propose that the deepening of peak dFe is caused by active, reversible exchange with a gravitationally sinking particulate phase through rapid adsorption/desorption (or aggregation/disaggregation for the colloidal phase). This reversible scavenging could occur onto material settling through the water column or onto hydrothermal pFe, but the matching descent rates for plume dFe and pFe (~5-10 m/y, or ~0.01-0.03 m/d) are three orders of magnitude slower than typical settling rates for marine aggregates (~17-200 m/d[43]), suggesting that dFe desorption:sorption rate ratios are high and/or that scavenging onto persistent hydrothermal pFe phases dominates dFe descent (Figure 2). The exchange must involve organically-complexed dFe pools, since dFe descent continues at a nearly constant rate down-plume (Figure 4), even as the concentration of ligand-bound dFe exceeds that of nanoparticulate Fe oxyhydroxides at distances >200 km from the SEPR (Sta. 21+; Figure 2, 6b). We hypothesize, on the basis of the carbon matrix surrounding Fe phases in the plume particles (Figure 5d-f), that this Fe exchange may be mediated by organic compounds binding dFe and pFe, via two potential mechanisms: hydrophobic attraction between pFe organic matrices and

organic Fe-ligand complexes, and/or "ligand-exchange" of Fe cations between dissolved ligands and the organic matrices of pFe. The coincidence of reversible dFe scavenging with the organic association of both dFe and pFe suggests a single mechanism for exchange between dissolved and particulate phases, reminiscent of the spontaneously assembling/disassembling marine gels common in the upper ocean and nepheloid layers[44]. Such an exchange-sinking mechanism would not apply to dMn because dMn is minimally complexed by organic matter in natural waters[2], and negligible Mn was observed in the colloidal fraction (Figure S4).

Implications for hydrothermal fluxes and scavenging **-** Our results suggest that while nanoparticulate Fe(III) oxyhydroxides dominate hydrothermally-sourced dFe speciation near the SEPR, isotopically heavy organic complexes dominate the hydrothermal dFe phase that persists throughout the distal SEPR plume, influencing the Pacific Ocean dFe inventory. The generality of this conclusion is supported by recent observations of heavy (+0.54±0.14‰) hydrothermally-sourced dissolved δ^{56}Fe values found >2000 km east of the SEPR axis at ~25°S in the Peru/Chile Basin[45]. However, our model-derived hydrothermal ligand-bound dFe concentrations (~0.3 nM) are much lower than those currently parameterized in modeling efforts focused on near-field vent geochemistry[8]. New global modeling efforts should seek to capture the vertical migration of dFe plumes to deeper isopycnals as they disperse (Figure 2) to improve estimates of hydrothermal-derived dFe upwelling to the surface ocean, and hence of Fe-fertilized primary production and associated carbon dioxide drawdown[8].

The decoupled speciation and transport pathways of hydrothermal pFe and pMn demonstrated here (Figure 2) have important implications for the oceanic budgets of the many dissolved elements in hydrothermal plumes[1] that sorb to the surfaces of Fe and Mn particles,

250 the “scavengers of the sea”[46]. Particle-reactive elements are numerous, spanning the periodic
251 table[5], but each has a distinct sorption affinity for Fe versus Mn particles[47], further complicated
252 by the pFe organic matrix reported here. The decoupled speciation, stabilization, and transport
253 pathways for Fe and Mn particles in hydrothermal plumes revealed by this study must directly
254 govern the fate and oceanic budgets of numerous scavenging-prone elements, in addition to Fe
255 and Mn.

256 More generally, the reversible scavenging model elucidated here represents a paradigm
257 shift for parameterizations of dFe scavenging in ocean models. Current global biogeochemical
258 Fe models invoke irreversible removal to particulate phases as the dominant abiotic dissolved-
259 particulate interaction[3,48] (with one exception that parameterized reversible scavenging[49]).
260 However, we report an Fe settling rate ~1000 times slower than typical marine aggregate
261 settling[43] (Figure 2), suggesting selective dFe scavenging onto the suspended hydrothermal pFe
262 phase and/or a large desorption-sorption rate ratio. Modeling of the Fe distributions presented
263 here (beyond the scope of this paper) will seek to reveal transformation rates that determine
264 the oceanic residence time of hydrothermally-sourced dFe. Future work should investigate
265 whether such reversible scavenging also occurs in other ocean regimes with high particulate Fe
266 loadings, including continental margins, high-dust regions, and benthic nepheloid layers;
267 ultimately, the global oceanic flux of dFe from all of these boundary systems should depend on
268 a balance between stabilization in the dissolved phase and reversible/irreversible scavenging
269 removal onto sinking particles. Perhaps most importantly, our observations of the decoupled
270 composition and settling rates of Fe and Mn suggest that the scavenging chemistry of different
271 elements is unique. Thus, the extent to which the aquatic chemistry of marine species is

controlled by organic versus inorganic components will determine how we model ocean processes as thermodynamic systems in the future.

Methods

Methods, including statements of data availability, are available in the online version of this paper.

References

1 German, C. R. & Seyfried, W. E. in *Treatise on Geochemistry, Second Edition* Vol. vol. 8 (eds H. D. Holland & K. K. Turekian) 191-233 (Elsevier, 2014).

2 Sunda, W. G. Feedback interactions between trace metal nutrients and phytoplankton in the ocean. *Frontiers in Microbiology* **3**, 204, (2012).

3 Moore, J. K. & Braucher, O. Sedimentary and mineral dust sources of dissolved iron to the world ocean. *Biogeosciences* **5**, 631-656, (2008).

4 Field, M. P. & Sherrell, R. M. Dissolved and particulate Fe in a hydrothermal plume at 9°45'N, East Pacific Rise: Slow Fe (II) oxidation kinetics in Pacific plumes. *Geochimica Et Cosmochimica Acta* **64**, 619-628, (2000).

5 German, C. R., Campbell, A. C. & Edmond, J. M. Hydrothermal scavenging at the Mid-Atlantic Ridge: Modification of trace element dissolved fluxes. *Earth and Planetary Science Letters* **107**, 101-114, (1991).

6 Wu, J., Wells, M. L. & Rember, R. Dissolved iron anomaly in the deep tropical-subtropical Pacific: Evidence for long-range transport of hydrothermal iron. *Geochimica Et Cosmochimica Acta* **75**, 460-468, (2011).

7 Fitzsimmons, J. N., Jenkins, W. J. & Boyle, E. A. Distal transport of dissolved hydrothermal iron in the deep South Pacific Ocean. *Proceedings of the National Academy of Sciences* **111**, 16654-16661, (2014).

8 Resing, J. A. *et al.* Basin-scale transport of hydrothermal dissolved metals across the South Pacific Ocean. *Nature* **523**, 200-206, (2015).

9 Noble, A. E. *et al.* Basin-scale inputs of cobalt, iron, and manganese from the Benguela-Angola front to the South Atlantic Ocean. *Limnology & Oceanography* **57**, 989-1010, (2012).

10 Fitzsimmons, J. N. *et al.* Partitioning of dissolved iron and iron isotopes into soluble and colloidal phases along the GA03 GEOTRACES North Atlantic Transect. *Deep-Sea Research II* **116**, 130-151, (2015).

11 Nishioka, J., Obata, H. & Tsumune, D. Evidence of an extensive spread of hydrothermal dissolved iron in the Indian Ocean. *Earth and Planetary Science Letters* **361**, 26-33, (2013).

12 Klunder, M. B., Laan, P., Middag, R., De Baar, H. J. W. & van Ooijen, J. C. Dissolved iron in the Southern Ocean (Atlantic sector). *Deep Sea Research Part II: Topical Studies in Oceanography* **58**, 2678-2694, (2011).

13 Hawkes, J. A., Connelly, D. P., Rijkenberg, M. J. A. & Achterberg, E. P. The importance of shallow hydrothermal island arc systems in ocean biogeochemistry. *Geophysical Research Letters* **41**, 2013GL058817, (2014).

14 Klunder, M. B., Laan, P., Middag, R., de Baar, H. J. W. & Bakker, K. Dissolved iron in the Arctic Ocean: Important role of hydrothermal sources, shelf input and scavenging removal. *Journal of Geophysical Research* **117**, C04014, (2012).

15 Yucel, M., Gartman, A., Chan, C. S. & Luther, G. W. Hydrothermal vents as a kinetically stable source of iron-sulphide-bearing nanoparticles to the ocean. *Nature Geoscience* **4**, 367-371, (2011).

16 Sands, C. M., Connelly, D. P., Statham, P. J. & German, C. R. Size fractionation of trace metals in the Edmond hydrothermal plume, Central Indian Ocean. *Earth and Planetary Science Letters* **319-320**, 15-22, (2012).

17 Gartman, A., Findlay, A. J. & Luther III, G. W. Nanoparticulate pyrite and other nanoparticles are a widespread component of hydrothermal vent black smoker emissions. *Chemical Geology* **366**, 32-41, (2014).

18 Bennett, S. A. *et al.* The distribution and stabilisation of dissolved Fe in deep-sea hydrothermal plumes. *Earth and Planetary Science Letters* **270**, 157-167, (2008).

19 Sander, S. G. & Koschinsky, A. Metal flux from hydrothermal vents increased by organic complexation. *Nature Geoscience* **4**, 145-150, (2011).

20 Hawkes, J. A., Connelly, D. P., Gledhill, M. & Achterberg, E. P. The stabilisation and transportation of dissolved iron from high temperature hydrothermal vent systems. *Earth and Planetary Science Letters* **375**, 280-290, (2013).

21 Feely, R. A. *et al.* Hydrothermal plume particles and dissolved phosphate over the superfast-spreading southern East Pacific Rise. *Geochimica et Cosmochimica Acta* **60**, 2297-2323, (1996).

22 Boström, K., Peterson, M. N. A., Joensuu, O. & Fisher, D. E. Aluminum-poor ferromanganoan sediments on active oceanic ridges. *Journal of Geophysical Research* **74**, 3261-3270, (1969).

23 Lupton, J. Hydrothermal helium plumes in the Pacific Ocean. *Journal of Geophysical Research* **103**, 15853-15868, (1998).

24 Black, E. E., Buesseler, K. O., Pike, S. M., Lam, P. J. & Charette, M. A. in *Ocean Sciences Meeting.*

25 Hautala, S. L. & Riser, S. C. A nonconservative β-spiral determination of the deep circulation in the Eastern South Pacific. *Journal of Physical Oceanography* **23**, 1975-2000, (1993).

26 Faure, V. & Speer, K. Deep circulation in the eastern South Pacific Ocean. *Journal of Marine Research* **70**, 748-778, (2012).

27 Toner, B. M. *et al.* Preservation of iron(II) by carbon-rich matrices in a hydrothermal plume. *Nature Geoscience* **2**, 197-201, (2009).

28 Cowen, J. P., Massoth, G. J. & Baker, E. T. Bacterial scavenging of Mn and Fe in a mid- to far-field hydrothermal particle plume. *Nature* **322**, 169-171, (1986).

29 Cowen, J. P., Massoth, G. J. & Feely, R. A. Scavenging rates of dissolved manganese in a hydrothermal vent plume. *Deep Sea Research Part A. Oceanographic Research Papers* **37**, 1619-1637, (1990).

30 Nealson, K. H., Tebo, B. M. & Rosson, R. A. Occurrence and mechanisms of microbial oxidation of manganese. *Advances in Applied Microbiology* **33**, 279-318, (1988).

31 Toner, B. M. *et al.* The Speciation of Particulate Iron and Carbon in the East Pacific Rise 15^{o}S Near-field Hydrothermal Plume and Underlying Sediments. *AGU Fall Meeting*, San Francisco, California, USA, (2014).

32 Dauphas, N. & Rouxel, O. Mass spectrometry and natural variations of iron isotopes. *Mass Spectrometry Reviews* **25**, 515-550, (2006).

33 Wells, M. L. & Goldberg, E. D. Marine submicron particles. *Marine Chemistry* **40**, 5-18, (1992).

34 Bennett, S. A. *et al.* Iron isotope fractionation in a buoyant hydrothermal plume, 5S Mid-Atlantic Ridge. *Geochimica Et Cosmochimica Acta* **73**, 5619-5634, (2009).

35 Dideriksen, K., Baker, J. A. & Stipp, S. L. S. Equilibrium Fe isotope fractionation between inorganic aqueous Fe(III) and the siderophore complex, Fe(III)-desferrioxamine B. *Earth and Planetary Science Letters* **269**, 280-290, (2008).

36 Morgan, J. L. L., Wasylenki, L. E., Nuester, J. & Anbar, A. D. Fe isotope fractionation during equilibration of Fe-organic complexes. *Environmental Science & Technology* **44**, 6095-6101, (2010).

37 Bruland, K. W., Orians, K. J. & Cowen, J. P. Reactive trace metals in the stratified central North Pacific. *Geochimica Et Cosmochimica Acta* **58**, 3171-3182, (1994).

38 Conway, T. M. & John, S. G. The cycling of iron, zinc and cadmium in the North East Pacific Ocean - Insights from stable isotopes. *Geochimica et Cosmochimica Acta* **164**, 262-283, (2015).

39 Radic, A., Lacan, F. & Murray, J. W. Iron isotopes in the seawater of the equatorial Pacific Ocean: New constraints for the oceanic iron cycle. *Earth and Planetary Science Letters* **306**, 1-10, (2011).

40 Gledhill, M. & Buck, K. N. The organic complexation of iron in the marine environment: a review. *Frontiers in Microbiology* **3**, 69, (2012).

41 Dick, G. *et al.* The microbiology of deep-sea hydrothermal vent plumes: ecological and biogeographic linkages to seafloor and water column habitats. *Frontiers in Microbiology* **4**, (2013).

42 Bennett, S. A. *et al.* Dissolved and particulate organic carbon in hydrothermal plumes from the East Pacific Rise, 9°50'N. *Deep Sea Research Part I: Oceanographic Research Papers* **58**, 922-931, (2011).

43 Honjo, S., Manganini, S. J., Krishfield, R. A. & Francois, R. Particulate organic carbon fluxes to the ocean interior and factors controlling the biological pump: A synthesis of global sediment trap programs since 1983. *Progress in Oceanography* **76**, 217-285, (2008).

44 Verdugo, P. *et al.* The oceanic gel phase: a bridge in the DOM–POM continuum. *Marine Chemistry* **92**, 67-85, (2004).

45 Fitzsimmons, J. N. *et al.* Dissolved iron and iron isotopes in the Southeastern Pacific Ocean. *Global Biogeochemical Cycles*, (in press).

46 Goldberg, E. D. Marine Geochemistry 1. Chemical Scavengers of the Sea. *The Journal of Geology* **62**, 249-265, (1954).

47 Koschinsky, A. & Hein, J. R. Uptake of elements from seawater by ferromanganese crusts: solid-phase associations and seawater speciation. *Marine Geology* **198**, 331-351, (2003).

48 Völker, C. & Tagliabue, A. Modeling organic iron-binding ligands in a three-dimensional biogeochemical ocean model. *Marine Chemistry* **173**, 67-77, (2015).

406 49 Parekh, P., Follows, M. J. & Boyle, E. Modeling the global ocean iron cycle. *Global*
407 *biogeochemical cycles* **18**, (2004).
408 50 Revels, B. N., Zhang, R., Adkins, J. F. & John, S. G. Fractionation of iron isotopes during
409 leaching of natural particles by acidic and circumneutral leaches and development of an
410 optimal leach for marine particulate iron isotopes. *Geochimica et Cosmochimica Acta*
411 **166**, 92-104, (2015).
412
413
414 **Acknowledgements**: We thank Kiefer Forsch and Alexandra Malinina for assistance with
415 particulate metal digestions and Ryan Bu for mass spectrometry support; Phoebe Lam for
416 leading the McLane pump team and designing the filter manifold used for STXM sample
417 collection; Sara Rauschenberg, Claire Parker, Cheryl Zurbrick, Laura Richards, Daniel Ohnemus,
418 and the McLane pump team for help sampling on the GP16 cruise; Josh Helgoe and Emily
419 Townsend for assistance with sample processing for dissolved δ^{56}Fe; David Kilcoyne for STXM
420 training and guidance, and Rebecca Sims and Brandi Cron for beamtime support; and Jim
421 Moffett and Greg Cutter for their cruise leadership on GP16, as well as the support of the
422 officers and crew of the R/V *Thomas G. Thompson*. Daniel Ohnemus and Benjamin Twining
423 participated in data quality control discussions and intercalibration of the particulate metal
424 measurements, and Joe Resing, Pete Sedwick, and Bill Jenkins provided access to their
425 published dissolved Fe, Mn, and ^{3}He datasets and participated in helpful conversations about
426 our data interpretation. This work was funded by the National Science Foundation (OCE-
427 1234827 to R.M.S. and C.R.G., OCE-1235248 to C.R.G., OCE-1232986 to B.M.T., and OCE-

1649435 and OCE-1649439 to S.G.J.). The Advance Light Source is supported by the Director, Office of Basic Energy Sciences, of the U.S. Department of Energy under contract No. DE-AC02-05CF11231.

Author Contributions:

J.N.F determined the digested particulate metal concentrations, led data interpretation, and wrote the manuscript. R.M.S., C.R.G., and B.M.T. co-proposed the particulate studies, and R.M.S., S.L.N., and C.R.G. collected samples on the GP16 cruise (C.R.G. as Chief Scientist). S.G.J. and C.M.M. made the Fe isotope measurements, and C.L.H. and B.M.T. made the synchrotron measurements. All authors helped to refine the interpretation and contributed to manuscript revisions.

Competing Financial Interest

The authors declare no competing financial interests.

Figure Captions

Figure 1: Interpolated concentrations and station map along the U.S. GEOTRACES GP16 Eastern Pacific Zonal Transect. (a) Station locations and names in relation to the South American continent and the East Pacific Rise (colors are bathymetry; green hues shallower), (b) excess ^{3}He concentrations in fmol/kg, (c) dissolved Fe concentrations (<0.2 µm, in nM), (d)

dissolved Mn concentrations (<0.2 µm, in nM), (e) particulate Fe (>0.45 µm, in nM), and (f) particulate Mn (>0.45 µm, in pM). Note that in each data panel a black line is indicated at 2500 m to highlight the deepening of the Fe plumes.

Figure 2: Illustration of Fe, Mn, and $^{3}He_{xs}$ transport and transformation along the SEPR hydrothermal plume. Physical plume bounds are indicated in grey, at representative non-linear distances off-axis (listed at bottom). Concentric circles represent relative peak concentrations of particulate and dissolved metals; circle sizes represent relative concentrations but are not quantitatively accurate between Fe, Mn, and $^{3}He_{xs}$. Pie diagrams show chemical speciation of dissolved Fe. Particulate Fe and Mn are removed through aggregation onto sinking particles from above (white arrows[43]) and through near-field self-aggregation of hydrothermally-sourced particles. Note that Fe descends relative to Mn and $^{3}He_{xs}$, which mix along slightly deepening isopycnals.

Figure 3: Relationship between excess ^{3}He and metal inventories in the dissolved and particulate phases in the SEPR hydrothermal plume (2200-3000 m). All stations are included with the exception of Sta. 18 (directly over vent). Sta. 20 is plotted as open circles for Mn because those points fall off of the distal plume trend[8]. Integrating between 2200-3000 m captures the entirety of the sinking Fe plume. Linear relationships between $^{3}He_{xs}$ and dissolved metals suggest that dissolved metal inventories are apparently conserved (controlled by mixing/dilution), while the exponential relationship between particulate metals and $^{3}He_{xs}$ indicates aggregative removal of particles to >3000 m depth

Figure 4: Depth of peak concentrations in the SEPR hydrothermal plume. Vertical bars indicate depths where concentrations were within 2.5% of maximum. The 27.737 line is the potential

density layer on which maximum $^{3}He_{xs}$ was emplaced at Sta. 20; this is the isopycnal surface on which all dissolved species should have traveled. Notably, Fe species deepened, falling below this isopycnal, while Mn species mixed along it. The label "dFe-Resing" indicates dFe maxima published previously[8], while "dFe-John" are independent, mass spectrometric dFe measurements reported here; we report both to show that the pattern of dFe descent is reproducible and unrelated to data error.

Figure 5: Scanning transmission X-ray microscopy (STXM) images, elemental maps, and spectra for representative plume particles (>0.2 μm). Transmission images (a) and (d) collected at 290 eV. Distribution of total carbon with optical density of (b) 1.8 and (e) 0.63. Distribution of total iron with optical density of (c) 2.6 and (f) 0.57. Note that (f) does not cover the whole of the area imaged in (d) and (e). (g) Carbon 1s XANES spectra for particulate organic carbon from Sta. 20-21. (h) Iron 2p XANES spectrum for particulate iron(III) from Sta. 20-21, compared to standard ferrihydrite. All scale bars 2 μm.

Figure 6: Dissolved and labile particulate δ^{56}Fe results for hydrothermal depths 2200-2800 m. (a) Constant labile particulate[50] δ^{56}Fe (-0.25±0.14‰) over a wide range of pFe concentrations suggests that pFe loss is controlled by non-fractionating, physical aggregation/disaggregation processes. (b) Dissolved δ^{56}Fe increases down-plume, modeled as mixing (black line) between a hydrothermal nanoparticulate Fe(III) oxyhydroxide end-member (-0.19‰) and an isotopically heavier ligand-bound phase (+0.66‰, 0.77 nM; background and hydrothermal FeL complexes). Errors in [Fe] and particulate δ^{56}Fe are smaller than data points (5% and 0.02-0.03‰, 2σSE, respectively). Errors for some Station 20 dissolved δ^{56}Fe were unusually high because of an incorrection dilution (light gray).

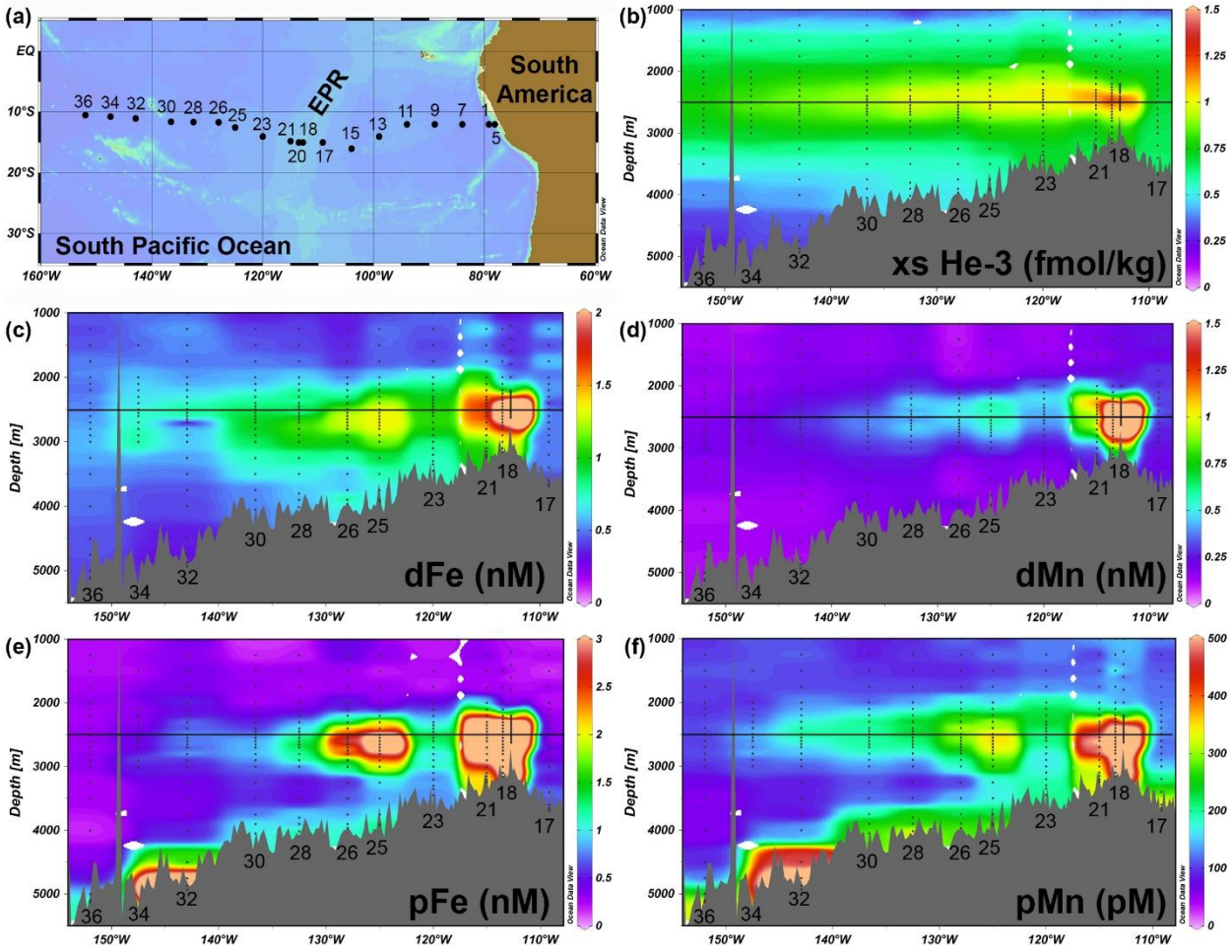
(a)
EQ
10°S
20°S
30°S
South America
EPR
South Pacific Ocean
36 34 32 30 28 26 25 23 21 18 20 17 15 13 11 9 7 1 5
160°W 140°W 120°W 100°W 80°W 60°W
(b)
xs He-3 (fmol/kg)
(c)
dFe (nM)
(d)
dMn (nM)
(e)
pFe (nM)
(f)
pMn (pM)
Depth [m]
1000 2000 3000 4000 5000
150°W 140°W 130°W 120°W 110°W
Ocean Data View

Figure 1

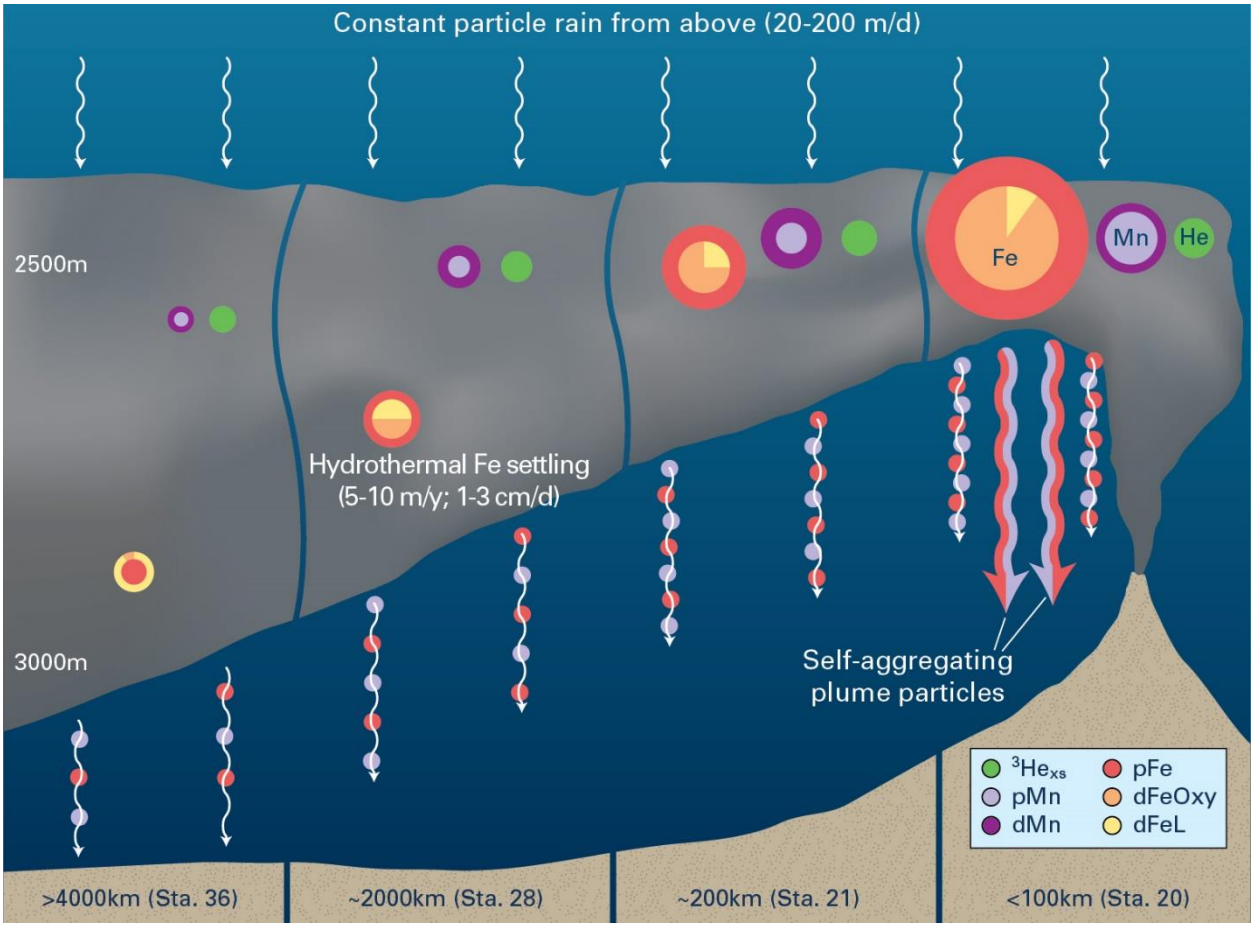

Figure 2 - **Please note that we would like to keep this figure as a 2-column figure, as it has critical components that would not be apparent in a 1-column figure.**

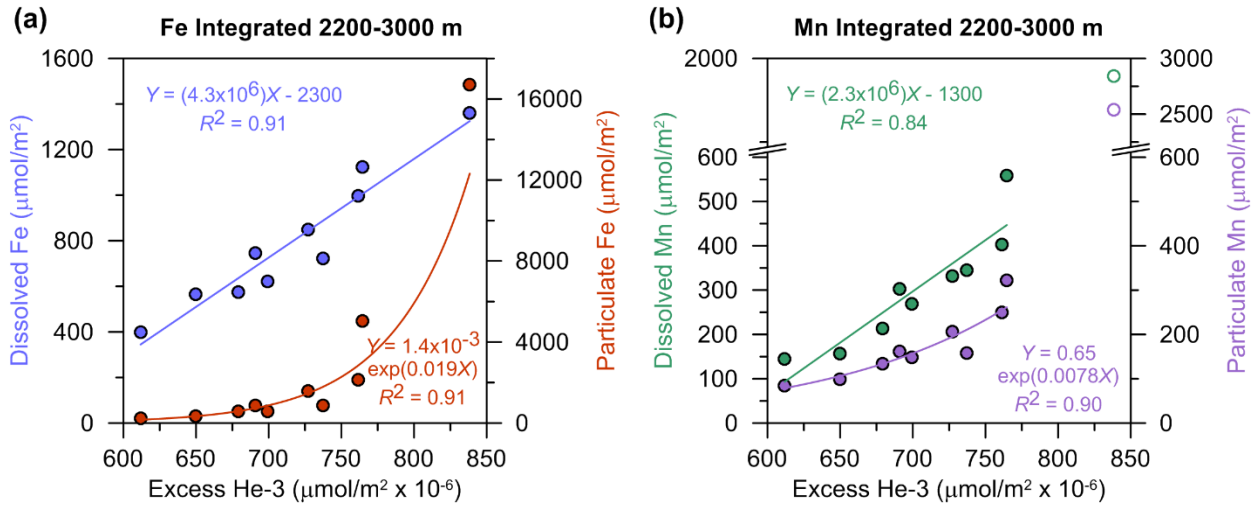

Figure 3

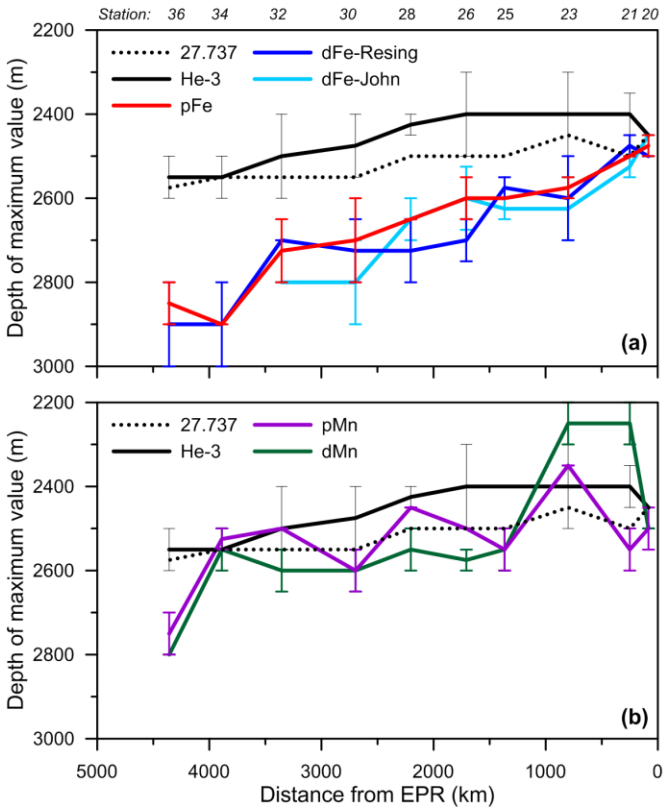
Station: 36 34 32 30 28 26 25 23 21 20
27.737
He-3
pFe
dFe-Resing
dFe-John
Depth of maximum value (m)
2200
2400
2600
2800
3000
(a)
27.737
He-3
pMn
dMn
Depth of maximum value (m)
(b)
5000
4000
3000
2000
1000
0
Distance from EPR (km)

Figure 4

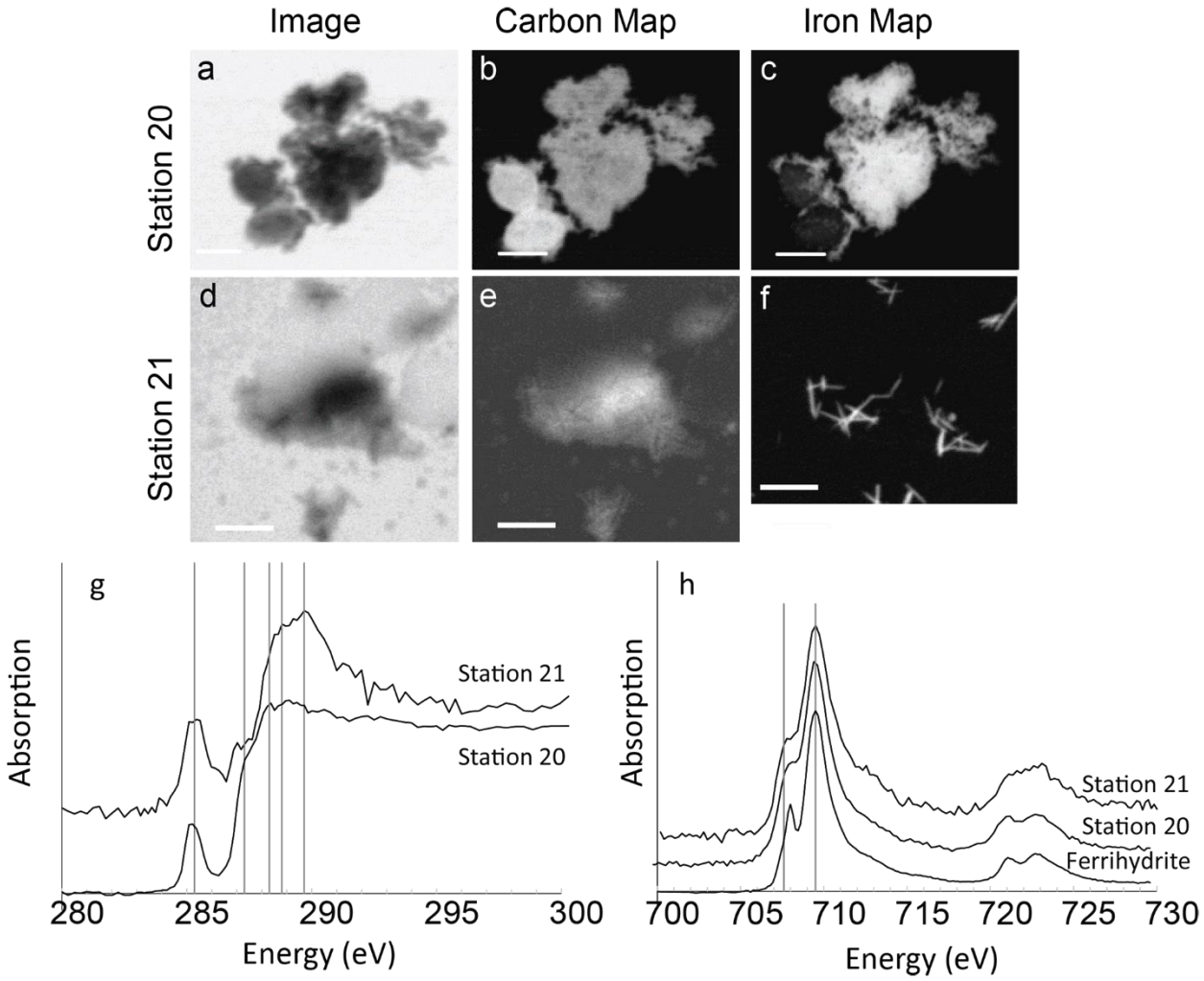
Image
Carbon Map
Iron Map
Station 20
Station 21
a
b
c
d
e
f
g
h
Absorption
Station 21
Station 20
280
285
290
295
300
Energy (eV)
Absorption
Station 21
Station 20
Ferrihydrite
700
705
710
715
720
725
730
Energy (eV)

Figure 5

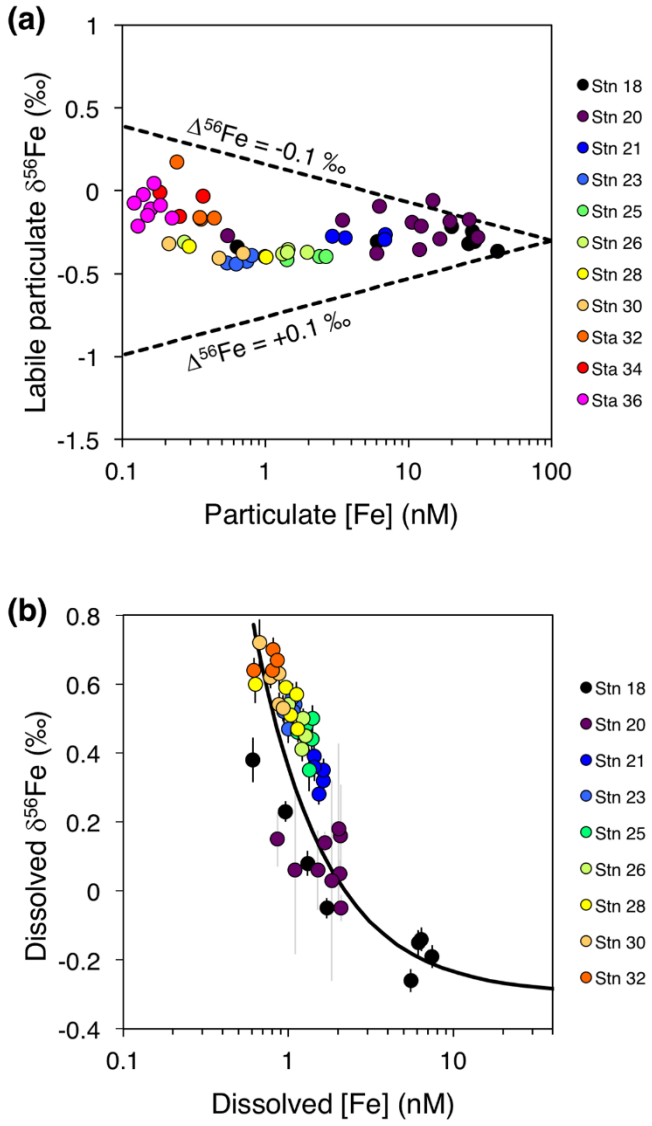
(a)
Labile particulate δ56Fe (‰)
Particulate [Fe] (nM)
Δ56Fe = -0.1 ‰
Δ56Fe = +0.1 ‰
Stn 18
Stn 20
Stn 21
Stn 23
Stn 25
Stn 26
Stn 28
Stn 30
Sta 32
Sta 34
Sta 36
(b)
Dissolved δ56Fe (‰)
Dissolved [Fe] (nM)
Stn 18
Stn 20
Stn 21
Stn 23
Stn 25
Stn 26
Stn 28
Stn 30
Stn 32

Figure 6

Online-Only Methods for:

Iron persistence in a distal hydrothermal plume supported by dissolved-particulate exchange

By: Jessica N. Fitzsimmons, Seth G. John, Christopher M. Marsay, Colleen L. Hoffman, Sarah L. Nicholas, Brandy M. Toner, Christopher R. German, and Robert M. Sherrell

Methods

Sample collection and processing - Trace metal-clean seawater samples were collected using the U.S. GEOTRACES sampling system consisting of 24 Teflon-coated GO-Flo bottles (General Oceanics) mounted onto an epoxy-coated aluminum frame that was deployed using Kevlar conducting cable[1]. GO-Flo bottles were pre-rinsed with a 24+ hour treatment of filtered surface seawater at the beginning of the cruise. At each station, the bottles were deployed open and tripped on ascent at 3 m/min. Upon recovery, the bottles were carried into a shipboard clean laboratory van that was over-pressurized with HEPA-filtered air for sampling under clean conditions. Immediately prior to and following deployments, the bottles were covered on both ends with plastic shower caps to avoid deck contamination.

During sub-sampling in the clean van, unfiltered salinity and nutrient samples were first taken from the GO-Flo bottles to create headspace, and then the bottles were inverted slowly three times to re-suspend any large particles that might have settled before sampling. GO-Flo bottles were then pressurized to ~0.7 atm with HEPA-filtered air, and filtration commenced using methods similar to those published previously[2]. Briefly, GO-Flo stopcocks were fitted with an acid-cleaned piece of Bev-a-Line tubing that fed into a polycarbonate elbow that was attached by Luer lock fitting to a 25 mm, polypropylene filter holder (Swinnex, Millipore) containing a 25 mm, acid-cleaned 0.45 µm polyethersulfone filter (Supor, Pall Gelman). Immediately prior to sampling, the headspace of the filter holder was flushed with seawater to evacuate any air bubbles in order to prevent air lock or occlusion of the filter surface area by air bubbles during sampling. Filtrate was directed into a plastic bucket, with the filter holders held approximately horizontal such that any residual headspace air bubbles would rise to the top of the filter holder, avoiding occlusion of the filter face. After filtration was complete (filter clogged to <1 drop of filtrate per second) or two hours had passed since the start of filtration, filtration was suspended by closing the stopcock on the GO-Flo bottle. Seawater volume passed through the filter was measured and recorded. The Swinnex filter holders were taken into a HEPA-filtered clean space,

and excess seawater was removed by gentle vacuum suction through the filter. The filter holders were then transferred in a sealed plastic bag to the HEPA-filtered "bubble" clean room in the ship's main lab. Working directly under a vertically flowing HEPA hood, the filter holders were opened, and the filter was removed using Tefzel forceps (held only by the edge of the filter). The non-sampled side of the filter was "blotted" by placing onto an acid-cleaned 47mm Supor filter to remove residual seawater by capillary action. Finally, the visibly dry filter was placed into an acid-cleaned polystyrene Petri Slide (EMD, Millipore) and stored at -20°C until analysis.

At the same time, a replicate set of GO-Flo bottles (tripped at the same depths as those sampled for suspended particles) was sampled for dissolved metals through a 0.2 µm Acropak-200 capsule filter (Pall) under the same pressure as described above. An acid-cleaned 1 L low density polyethylene (LDPE) plastic bottle was filled after three 10% volume rinses for Fe concentration and isotope measurements. Additionally, at a subset of depths a 4 L bottle was filled for ultrafiltration separation of soluble and colloidal metals. Ultrafiltration proceeded immediately by cross flow filtration (single-pass mode) across a 10 kDa regenerated cellulose membrane (Pellicon XL PLCGC)[3], with initial >200 mL ultrafiltrate discarded as rinse.

Particulate Analytical Methods – Particulate samples were analyzed in the Sherrell laboratory at Rutgers University. Frozen filters were cut in half using a ceramic rotary blade; a filter-cutting template was illuminated on a light table for guidance during cutting, and filter cutting error performed on blank filters was found to be ≤2% by weight. One filter half was used for sample digestion (reported here), and the other filter half was used for archiving or for acid leaching of "labile" metals (not reported). For digestion, filter halves were placed into the bottom of acid-clean 15 mL PFA vials (Savillex), and 0.4 mL of Milli-Q ultrapure water was added to the top. Once fully wetted, the filter half was pulled up the side of the vial and adhered to the wall, curved edge toward bottom of vial. Then 0.6 mL of a solution containing 16.7% (v/v) hydrofluoric acid (HF, Optima grade, Fisher) and 83.3% (v/v) nitric acid (HNO_3, Optima grade, Fisher) was added by pipet to each vial, aiming at the adhered filter half. The final digestion acid mixture was thus 1.0 mL of a solution containing 10% HF and 60% HNO_3 by volume. The vial was then capped tightly and placed on a Teflon hotplate at least 2 cm from other vials. These "bombs" were refluxed at 135°C for 4 hours. After cooling, solution was gathered to the bottom of the vials, lids were removed, and the digest solution was evaporated until ~5-10 µL of solution remained. At that point, 100 µL of concentrated HNO_3 was added, and the solution was re-evaporated until ~5-10 µL of solution remained. The additional HNO_3 dry-down encourages volatilization removal of HF. Evaporating to dryness was avoided in order to prevent "baking" sample residue onto the Teflon surface, to aid in complete re-dissolution, and to minimize carry-over to subsequent sample digestions upon vial reuse. Finally, the remaining droplet was brought up in 3.0 mL of 5% HNO_3 (v/v) and transferred to a 15mL acid-cleaned polypropylene centrifuge tube for archiving and analysis.

Particulate Fe analysis was completed in medium resolution on a Thermo Element 1 inductively coupled plasma mass spectrometer (ICP-MS), employing an Apex and ACM sequential desolvation system (ESI) to reduce molecular oxide ion formation. Sample solutions were diluted five times from the archived digest solutions (to reduce chemical matrix) and were

quantified using a nine-point standard curve with an identical acid matrix to that of samples and bracketing the concentration range of the samples, run at the beginning and end of each analytical session. Single-point standard additions were also run every ten samples to check for accuracy, and analytical replicates were made every ten samples to monitor analytical precision. Particulate Fe was measured on both ^{56}Fe and ^{57}Fe, and concentration data for each were found to be indistinguishable, raising confidence in the analytical Fe measurement.

After correction for dilution and division by equivalent seawater volume filtered through the half-filter, the Fe concentrations in seawater were corrected for process blank. The process blanks consisted of Supor filters through which ~2.0 L of 0.2 µm-filtered seawater were passed during sampling at sea. Process blanks were collected from a variety of locations and depths throughout the cruise (n=18); no trend in these blanks as a function of particle concentration in the seawater was observed, suggesting that particles smaller than 0.2 µm did not contribute significantly to the elemental composition of the process blank filter. These process blank filters were cut and digested as for normal samples, and the absolute moles of each element were corrected for elemental contributions from residual seasalt using the Na data, assuming that all Na was derived solely from seasalt and using the mean seawater ratio of all measured elements to Na. The median seasalt-corrected process blank for each element was then subtracted from each particle concentration.

External accuracy in the particulate Fe measurement was assessed by the digestion of two certified reference materials: BCR-414 (plankton) and PACS-2 (a marine sediment). Recovery of 10 mg of these reference materials by the methods described above was 100±8% (n=14) for BCR-414 and 89±8% (n=8) for PACS-2, indicating excellent analytical accuracy. A complete intercalibration for Fe and the rest of the element suite analyzed in this dataset can be found on BCO-DMO (http://www.bco-dmo.org/dataset/639847).

Fe Isotope Analytical Methods – Fe stable isotope ratios (δ^{56}Fe) and concentrations were measured using double-spike ICP-MS. Dissolved δ^{56}Fe and Fe concentrations were made on 1L seawater samples according to published methods[4]. Briefly, seawater was acidified to pH 1.7 for at least two months before sample processing. Samples were then amended with a double spike containing roughly equal amounts of ^{57}Fe and ^{58}Fe. Fe (as well as Zn and Cd) was extracted from the seawater onto Nobias PA-1 chelating resin (Hitachi) while raising the pH to 6-6.5. Extracted metals were eluted from the Nobias resin with 5% HNO_3, and purified by anion exchange chromatography. This method is associated with blanks of ~0.3 ng Fe and yields analytical errors of ~0.03 to 0.05 ‰ for deep-ocean seawater samples such as these.

Particulate samples for Fe stable isotope analysis were collected using in situ battery-powered pumps (McLane WRT-LV), employing a modified dual-flow configuration and deployed on a trace-metal clean hydrowire[5,6]. Particulate material was collected by pumping seawater (average volume ~400 L) through paired 0.8 µm polyethersulfone (Supor), 142 mm diameter filters loaded behind a 51 µm polyester pre-filter. Subsamples were taken from the 0.8 – 51 µm size fraction material by cutting a 1/16th section of the upper 0.8 µm Supor filter, using a ceramic rotary blade.

Ligand-leachable (labile) pFe concentrations and δ^{56}Fe were determined following application of an oxalate-EDTA leach at pH 8[7]. Each filter section was loosely folded and placed in a 2 mL polyethylene vial, to which 1 mL of oxalate-EDTA reagent was added. The sealed vials were then heated at 90 °C for two hours. Each leachate was then passed through a polypropylene syringe filter (0.45 µm) to remove any loose particles from the solution. Subsamples of leachate were diluted 20-fold using 0.1 M HNO_3 and iron concentrations measured on a Thermo Scientific Element II sector field ICP-MS. Using this measured iron as a guide, an aliquot of each leachate sample was spiked with a ^{57}Fe and ^{58}Fe double spike solution to give a 1:2 ratio of natural to spike iron. Spiked samples were evaporated to dryness, heated at 200 °C with concentrated HNO_3 and H_2O_2 to dissolve organic material, then dried down again and reconstituted in 10 M HCl + 0.01% H_2O_2. Samples were then purified by anion exchange chromatography. Samples were corrected for reagent blank contribution to both concentration and δ^{56}Fe as described in Revels et al. [7].

Observed labile δ^{56}Fe was compared to theoretical predictions of particulate δ^{56}Fe with different fractionation factors (Fig. 6). We assumed a starting pool of 100 nM pFe with a δ^{56}Fe of -0.3 ‰. Particulate δ^{56}Fe was then calculated for various Fe concentrations assuming that pFe was lost with an isotope effect (Δ^{56}Fe) of either +0.1 ‰ or -0.1 ‰, according to Rayleigh distillation, such that

$$\delta^{56}Fe_{particulate} = -0.3 + \Delta^{56}Fe \cdot \ln F$$

where F is the fraction of the original 100 nM pFe that remains in the particulate phase.

The full dissolved δ^{56}Fe data set can be found at http://www.bco-dmo.org/dataset/643809. The full particulate δ^{56}Fe data set can be found at http://www.bco-dmo.org/dataset/669178.

Synchrotron Analytical Methods – Plume particles for synchrotron-based STXM imaging and C and Fe XANES were collected by in situ filtration using McLane pumps[5] and a custom-built filter manifold for holding acid-cleaned 0.2 µm polycarbonate filters. Shipboard, the filter holders were opened in a Coy anaerobic chamber set up in a HEPA-filtered "bubble." All filters were handled under 5% H_2 and 95% N_2 atmosphere. Residual seawater was removed from the filter holders by pulling 2 mL of deoxygenated ultrapure water through the filters using a vacuum pump. The filters were then placed in plastic vials containing ~0.5 mL of deoxygenated ultrapure water for resuspension of particles. The vials were then sealed in Mylar-aluminum laminate bags, removed from the anaerobic chamber, and frozen until analysis.

STXM data collection was performed at the Advanced Light Source, Lawrence Berkeley National Laboratory, Berkeley, CA, USA, on beamline 5.3.2.2[8] for plume depths at Sta. 20 (2550 m water depth, GT 8705) and Sta. 21 (combined GT 8885, 8884, 8879, for 2000, 2300, and 3230 m water depths, respectively). Using an adapted version of a published method[9], the plume particles suspension was defrosted and shaken. Then, in an anaerobic chamber, ~1 µL was deposited on a silicon nitride membrane (Silson Ltd.) and dried at room temperature; this preparation resulted in dispersed particles with no sea salt precipitates. Optical density (OD) images were created from X-ray images recorded at energies just below and at the C 1s (280, 290

eV) and Fe 2p (700, 710 eV) absorption edges. XANES spectra were collected from image sequences collected at energies spanning the C 1s and Fe 2p absorption edges (280-340 eV for C, 685-745 eV for Fe). Theoretical spatial and spectral resolutions were 20 nm and ± 0.1 eV, respectively. All measurements were performed at ambient temperature and < 1 atm He. Calibration at the C 1s edge was accomplished with the 3s (292.74 eV) and 3p (294.96 eV) Rydberg transitions of gaseous CO_2. All data processing was carried out with the IDL *aXis2000* software package (http://unicorn.mcmaster.ca/aXis2000.html).

Data usage from the literature – The dissolved Mn data used in this paper were taken from Resing et al.[10]. The ^{3}He data were also updated from the same paper with additional station coverage and improved corrections to attain the non-atmospheric ($^3He_{xs}$) component, as follows:

$$^3He_{xs} = {}^3He_{meas} - {}^3He_S - {}^3He_A$$

where the measured ^{3}He concentration ($^3He_{meas}$) is calculated from the measured isotope ratio anomaly (δHe in %) and measured helium concentration ([He]) as:

$$^3He_{meas} = 1.384 \times 10^{-6} (1 + \delta He/100)*[He]$$

and is corrected for the solubility abundance of He (^3He_S), which is a function of the salinity and temperature of the seawater C_SHe and the temperature-dependent fractionation factor of $^3He/^4He$ (α_S = 0.98-0.99):

$$^3He_S = \alpha_S \times 1.384 \times 10^{-6} \times C_SHe$$

and is also corrected for the amount of ^{3}He injected from the air (^3He_A), which is inferred from the super-saturation of neon (Ne) and the atmospheric He/Ne molar ratio (0.28823):

$$^3He_A = 1.384 \times 10^{-6} \times 0.28823 \times (Ne - C_SNe).$$

The dissolved Fe data reported in this paper are the high resolution data collected at sea by Dr. Peter Sedwick[10] (PS, Old Dominion University) after corrections for accuracy using the lower resolution but higher accuracy, lab-based data collected on a subset of samples using the aforementioned methods (SGJ). A linear correlation between the data of PS and SGJ at Stations 17-36 resulted in an R^2 of 0.96; the SGJ data set had 188 datapoints over this range, while the PS dataset had 440 points (41% data coverage, distributed nearly every other sample to make the regression).

Data Availability – The dissolved and particulate concentration and isotope ratio data that support the findings of this study are available on the Biological and Chemical Oceanography Data Management Office (BCO-DMO), http://www.bco-dmo.org/project/499723.

Supplemental References

1 Cutter, G. A. & Bruland, K. W. Rapid and noncontaminating sampling system for trace elements in a global ocean surveys. *Limnology & Oceanography: Methods* **10**, 425-436, (2012).

2 Planquette, H. & Sherrell, R. M. Sampling for particulate trace element determination using water sampling bottles: methodology and comparison to in situ pumps. *Limnology and Oceanography: Methods* **10**, 367-388, (2012).

3 Fitzsimmons, J. N. & Boyle, E. A. Assessment and comparison of Anopore and cross flow filtration methods for the determination of dissolved iron size fractionation into soluble and colloidal phases in seawater. *Limnology & Oceanography: Methods* **12**, 244-261, (2014).

4 Conway, T. M., Rosenberg, A. D., Adkins, J. F. & John, S. G. A new method for precise determination of iron, zinc, and cadmium stable isotope ratios in seawater by double-spike mass spectrometry. *Analytica Chimica Acta* **793**, 44-52, (2013).

5 Lam, P. J., Ohnemus, D. C. & Auro, M. E. Size-fractionated major particle composition and concentrations from the US GEOTRACES North Atlantic Zonal Transect. *Deep Sea Research Part II: Topical Studies in Oceanography* **116**, 303-320, (2015).

6 McDonnell, A. M. P. *et al.* The oceanographic toolbox for the collection of sinking and suspended marine particles. *Progress in Oceanography* **133**, 17-31, (2015).

7 Revels, B. N., Zhang, R., Adkins, J. F. & John, S. G. Fractionation of iron isotopes during leaching of natural particles by acidic and circumneutral leaches and development of an optimal leach for marine particulate iron isotopes. *Geochimica et Cosmochimica Acta* **166**, 92-104, (2015).

8 Kilcoyne, A. L. D. *et al.* Interferometer-controlled scanning transmission X-ray microscopes at the Advanced Light Source. *Journal of Synchrotron Radiation* **10**, (2003).

9 Toner, B. M. *et al.* Preservation of iron(II) by carbon-rich matrices in a hydrothermal plume. *Nature Geoscience* **2**, 197-201, (2009).

10 Resing, J. A. *et al.* Basin-scale transport of hydrothermal dissolved metals across the South Pacific Ocean. *Nature* **523**, 200-206, (2015).

Supplementary Information for:

Iron persistence in a distal hydrothermal plume supported by dissolved-particulate exchange

By: Jessica N. Fitzsimmons, Seth G. John, Christopher M. Marsay, Colleen L. Hoffman, Sarah L. Nicholas, Brandy M. Toner, Christopher R. German, and Robert M. Sherrell

Materials:

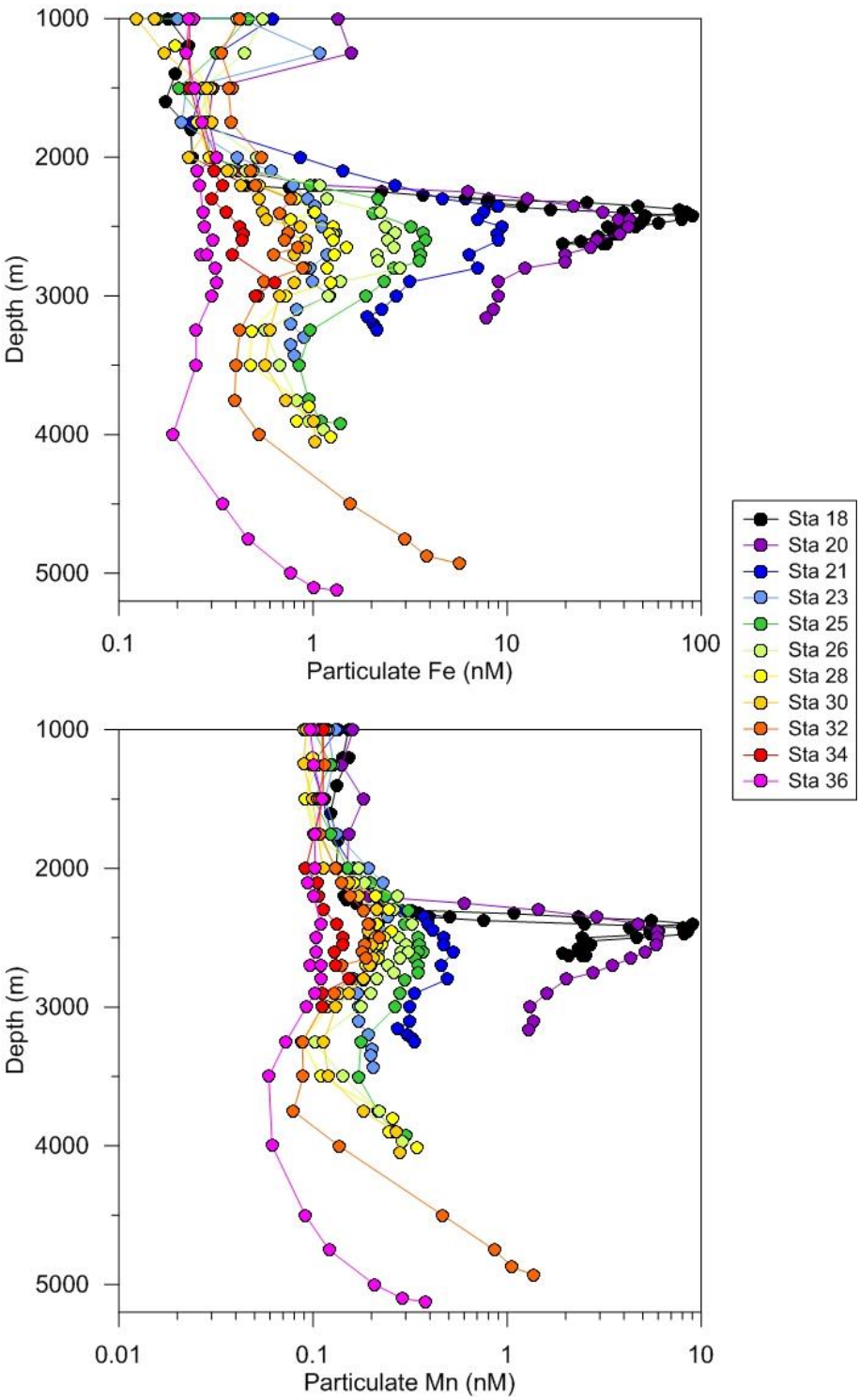

Figure S1. Depth profiles of particulate Fe (top) and Mn (bottom) concentrations on a log scale for each station on GP16 in the hydrothermal plume. Note that the Mn concentration scale is an order of magnitude lower than the Fe concentration scale.

2. Kinetics of particulate Fe removal from the hydrothermal plume

Hydrothermal Fe and Mn particles were non-conservatively removed from the plume, as attested by their non-linear relationships with the conservative hydrothermal tracer $^{3}He_{xs}$ (Figure 3). To attempt to resolve the mechanism of aggregative removal, kinetics testing on the particulate metal data was conducted to determine whether the aggregative removal occurs predominantly by self-collision (second order) or by collision with a sinking particulate phase from shallower in the water column (first order).

Self-aggregation kinetics should occur as a second order function of the hydrothermal particle concentration[1], such that the removal rate is a quadratic function of the particulate metal concentration (two like hydrothermal particles must collide to aggregate):

$$\frac{\partial[C]}{\partial t} = -2k\,[C]^2$$

where *k* is the removal rate constant, *[C]* is the concentration of any element, and *t* is time. When this removal rate equation is integrated at steady state, a linear relationship between the natural log of the concentration and time can be expected:

$$\frac{1}{[C]} = 2kt + \frac{1}{[C]_0}$$

where $[C]_0$ is the starting concentration of the element in the hydrothermal plume at emplacement. When we evaluated our particulate metal inventories (integrated 2200-3000 m depth) using this technique (Figure S2, top panel), our observations were instead better fit by a first order kinetic model (Figure S2, bottom panel), where the removal rate is a linear function of the particulate metal concentration:

$$\frac{\partial[C]}{\partial t} = -k\,[C]$$

$$\ln[C] = -kt + \ln[C]_0$$

The first order dependence of particulate Fe and Mn removal is consistent with an aggregative removal mechanism involving collision of hydrothermal particles with sinking aggregates from the surface ocean.

However it is worth noting that the greatest deviation from linearity in the first-order kinetic tests occurred nearest the vents (especially station 20). Thus, nearer to the vents where hydrothermal particulate concentrations are highest, self-collision aggregative mechanisms may dominate. Our sampling resolution did not increase nearer the SEPR axis, and thus we cannot further prove this quantitatively due to lack of data.

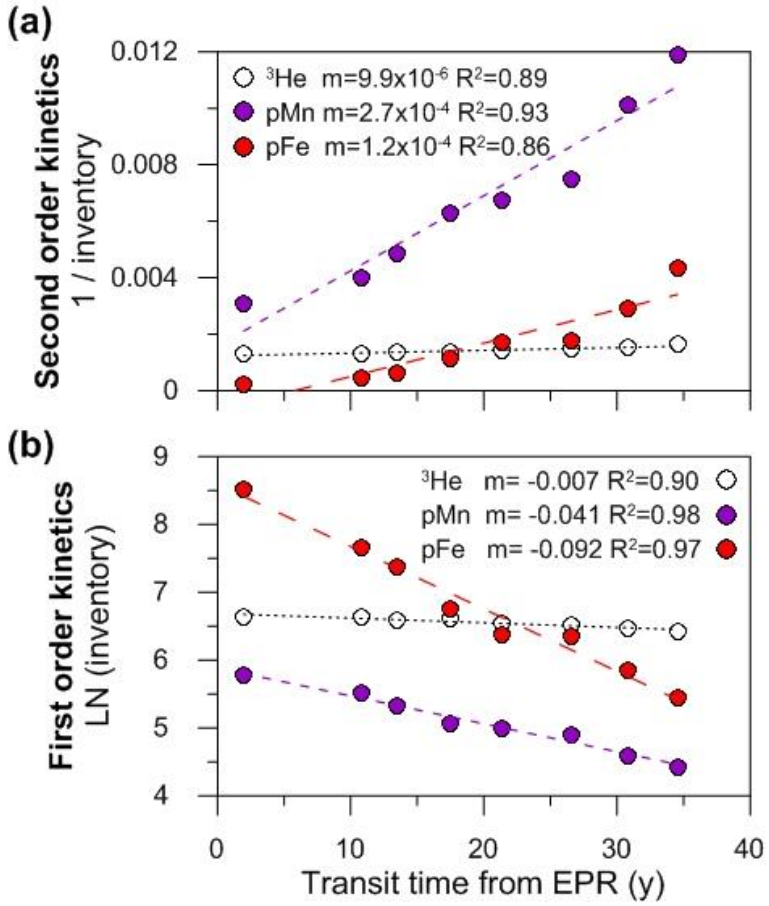

Figure S2: Kinetic rate order assessment for particle metal removal from the distal hydrothermal plume (Stations 21-36). Transit time was calculated using the 0.4 cm/s advection rate calculated using ^{227}Ac inventories[2] and distance from the 15°S EPR. The negligible slope from the ^{3}He relationships reveals the second (a) and first (b) order dependence of the conservative mixing/advection terms in the circulation of the hydrothermal plume. (a) Self-aggregative removal of hydrothermal materials are modeled as a second order function of elemental concentration. The slight curvature in the second order kinetic relationships for particulate Fe and Mn suggests that second order kinetics (aggregation by hydrothermal-self aggregation) is not the best model of particulate removal rate for the plume as a whole. (b) Instead first order kinetics (aggregation of hydrothermal particles onto sinking particles from the surface ocean) is an improved model of how hydrothermal particles are removed from the plume. In this model, hydrothermal elements are modeled as a first order function of elemental concentration. Station 23 data are excluded from these kinetics plots because of their anomalous plume behavior.

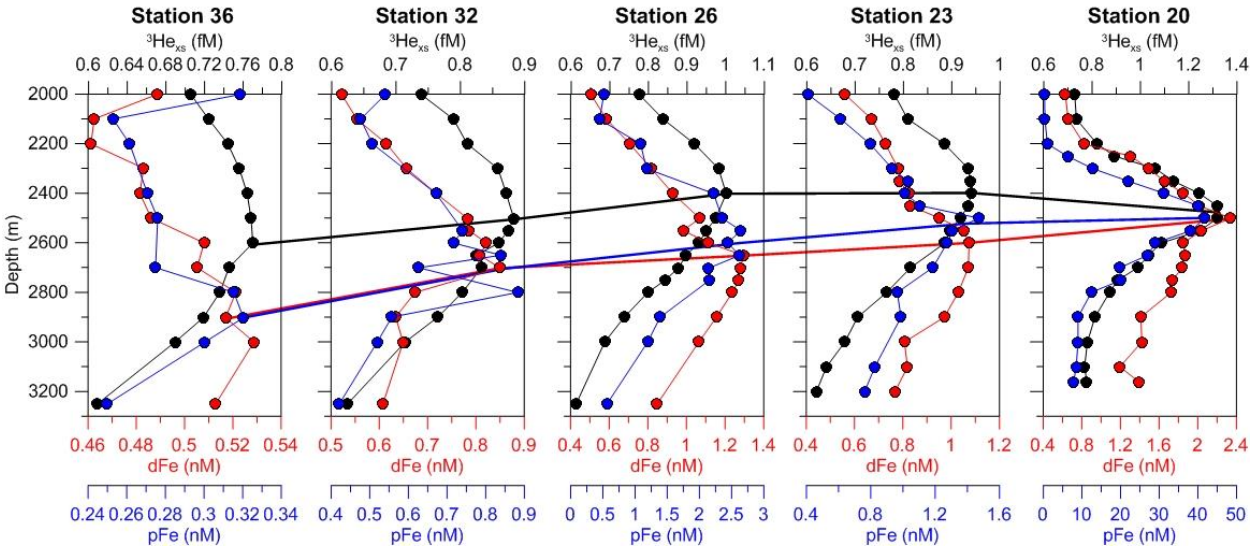

Figure S3: Descent of Fe in the hydrothermal plume from the perspective of the full profiles. Dissolved Fe is shown in red, particulate Fe in blue, and excess He-3 in black. Note that the concentration scale changes in each panel and often does not go to zero. The bolded lines connect the maximum values for each profile to the maximum values from the flanking profiles. Both Fe phases sink relative to $^3He_{xs}$.

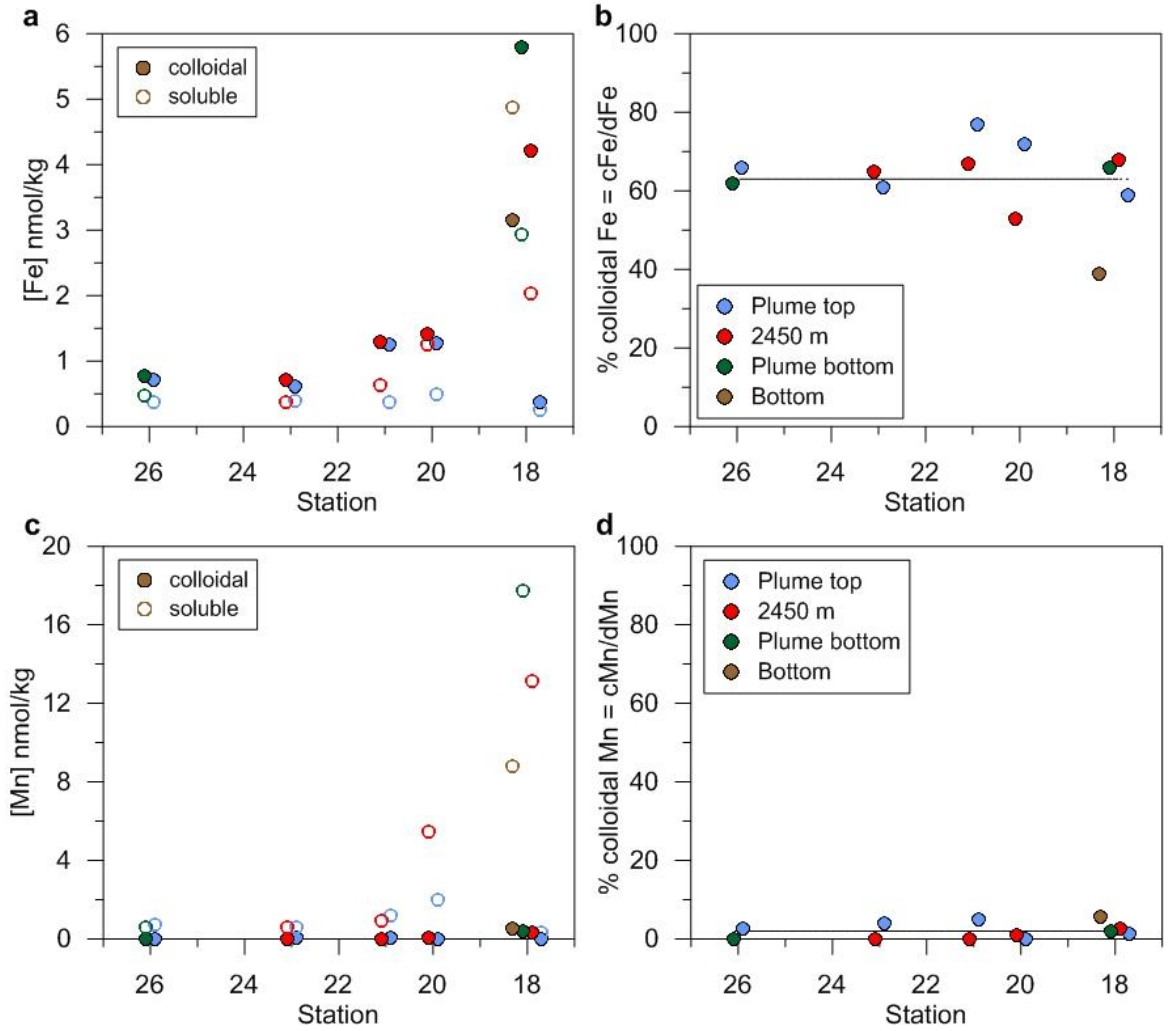

Figure S4: Colloidal Fe is a significant component of dissolved Fe in the plume, while colloidal Mn is an insignificant fraction of total dissolved hydrothermal plume Mn. (a) Measured concentrations of soluble Fe (<10 kDa ~ 0.003 µm; open symbols) and colloidal Fe (0.003-0.2 µm; closed symbols) are shown as a function of station number. Depths at the top of the plume (≤ 2350 m) are shown in blue, in the plume core (~2450 m) are shown in red, at the bottom of the plume (≥2500 m) are shown in green, and near-seafloor are shown in brown. (b) The percent contribution to dissolved Fe by colloidal Fe (cFe/dFe) was very constant across all stations and depths at 63+10% (indicated by the dotted line). Note that physical speciation into soluble vs. colloidal size fractions does not define inorganic vs. organic chemical speciation; marine Fe colloids can be inorganic or organically complexed. (c) Measured concentrations of soluble Mn (<0.003 µm; open symbols) and colloidal Mn (0.003-0.2 µm; closed symbols) are shown as a function of station number. (d) The contribution to dissolved Mn by colloidal Mn species (cMn/dMn) was very constant across all stations and depths at 2±2% (indicated by the dotted line); there were negligible Mn colloids.

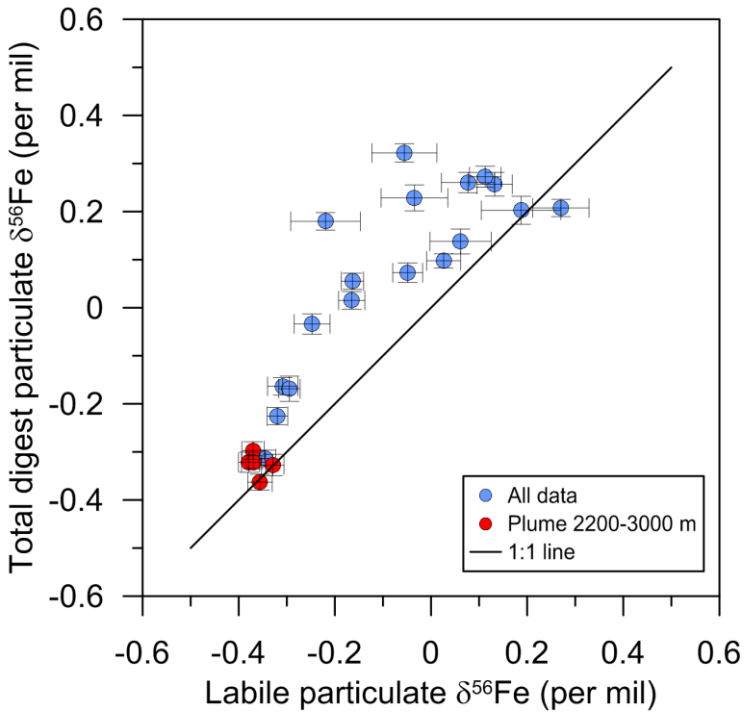

Figure S5: The δ^{56}Fe of labile pFe and total digest pFe are identical within error in plume samples at Station 26. The particulate δ^{56}Fe reported in Figure 6a are for the labile pFe phase (analyzed using an oxalate-EDTA leach at pH 8, see Online Methods). Evidence from treatment of different natural particle types[3] and samples collected during North Atlantic GEOTRACES[4] indicate that the ligand-leach treatment promotes dissolution of biological Fe, Fe oxyhydroxides that precipitate during oxidation of Fe(II) released from hydrothermal plumes and sediment porewaters, and Fe loosely bound/adsorbed to clay particles – i.e. the pFe most likely to be bioavailable. At Station 26, the labile pFe δ^{56}Fe data were compared to the total digest pFe δ^{56}Fe data, which includes additionally all lithogenic/refractory Fe (blue symbols). At plume depths (red symbols), the labile and total digest δ^{56}Fe values agreed, consistent with prior assessments that the oxalate-EDTA treatment accesses hydrothermal pFe forms. These data support our use of labile pFe δ^{56}Fe data to reveal hydrothermal Fe transformations in the SEPR plume (Figure 6).

6. Supplemental References

1 Stumm, W. & Morgan, J. J. *Aquatic Chemistry: Chemical Equilibria and Rates in Natural Waters*. 3rd edn, (John Wiley & Sons, 1996).

2 Hammond, D. E. *et al.* 227Ac in the Deep South Pacific along the Peru-Tahiti GEOTRACES Transect: Mixing and Transport Rates. *Ocean Sciences Meeting*, New Orleans, Louisiana, (2016).

3 Revels, B. N., Zhang, R., Adkins, J. F. & John, S. G. Fractionation of iron isotopes during leaching of natural particles by acidic and circumneutral leaches and development of an optimal leach for marine particulate iron isotopes. *Geochimica et Cosmochimica Acta* **166**, 92-104, (2015).

4 Revels, B. N., Ohnemus, D. C., Lam, P. J., Conway, T. M. & John, S. G. The isotopic signature and distribution of particulate iron in the North Atlantic Ocean. *Deep Sea Research Part II: Topical Studies in Oceanography* **116**, 321-331, (2015).